

# ENSEMBLE FORECASTS AND THE PROPERTIES OF FLOW-DEPENDENT ANALYSIS-ERROR COVARIANCE SINGULAR VECTORS

Thomas M. Hamill<sup>1</sup>, Chris Snyder<sup>2</sup>, and Jeffrey S. Whitaker<sup>3</sup>

<sup>1</sup>*University of Colorado and NOAA-CIRES Climate Diagnostics Center, Boulder, Colorado*

<sup>2</sup>*National Center for Atmospheric Research, Boulder, Colorado*

<sup>3</sup>*NOAA-CIRES Climate Diagnostics Center, Boulder, Colorado*

1 May 2002

submitted to *Monthly Weather Review*

DRAFT

\* The National Center for Atmospheric Research is sponsored by the National Science Foundation

*Corresponding author address:* Dr. Thomas M. Hamill, NOAA-CIRES CDC, R/CDC 1, 325  
Broadway, Boulder, CO 80305-3328. e-mail: hamill@cdc.noaa.gov

## ABSTRACT

Flow-dependent analysis-error covariance singular vectors (AEC SVs) are calculated in a dry, primitive equation global model. Sets of 400-member ensembles of analyses were generated by an ensemble square-root filter data assimilation system. A sparse network of simulated rawinsonde observations were assimilated, and a perfect model was assumed. Ensembles of 48-h forecasts were also generated from these analyses. The structure of evolved singular vectors were determined by finding the linear combination of the forecast ensemble members that resulted in the largest forecast-error variance, here measured in a total-energy norm north of 20° N latitude. The same linear combination of analyses specifies the initial-time structure that should evolve to the forecast singular vector under assumptions of linearity of error growth.

The structure of these singular vectors more closely resembles the structure of Hessian singular vectors than the total-energy singular vectors (TE SVs) currently used by the European Centre for Medium-Range Weather Forecasts to initialize their ensemble forecasts. The AEC SVs have maximum amplitude in mid-latitudes near the tropopause, both at the initial and final times. The AEC SVs are synoptic in scale and, for this model, do not appear to be geographically localized. This contrasts with TE SVs, which start off relatively smaller in scale and with amplitudes typically largest in the lower- to mid-troposphere.

The theoretically appropriate choice of initial norm for generating singular vectors is a flow-dependent analysis-error covariance norm such as demonstrated here. Consequently, the difference in structure between these singular vectors and ECMWF's TE SVs suggest that operational ensemble forecasts could be improved by changing the type of singular vector used to generate initial perturbations. The structure of the perturbations is likely to be especially important for short-range ensemble forecasts, where the structure of the forecast ensemble is more closely tied to the analysis ensemble. The difference between the structure of AEC SVs and TE SVs also

has implications for adaptive observing; these results suggest that the largest forecast improvement should come from observing near the jet level, not in the middle troposphere.

## 1. INTRODUCTION

Though ensemble forecasting has been operational in the U.S., Europe, and Canada for nearly a decade now, no clear consensus has yet evolved on the best practical method for generating initial conditions for these ensemble forecasts. In principle, it is understood from the Liouville equation (e.g., Ehrendorfer 1994) that the samples should be drawn from the probability distribution of analysis states, regardless of whether they should be drawn randomly or non-randomly. However, this analysis-error probability distribution can be highly flow-dependent and difficult to calculate. Analysis errors may be quite small in the region of, say, an amply observed blocking high, much larger in the region of a sparsely observed storm track. A computationally efficient method for generating sets of initial conditions that are consistent with flow-dependent analysis-error statistics has yet to be demonstrated with an operational weather forecast and data assimilation system. As a consequence, each of the operational numerical weather prediction centers have embraced different approaches to generate initial conditions for their ensemble forecasts. The European Centre for Medium-Range Weather Forecasts (ECMWF) have used “singular vector” perturbations (Molteni et al. 1996); the National Centers for Environmental Prediction (NCEP) use a “breeding” method (Toth and Kalnay 1993, 1997); and at the Canadian Meteorological Centre (CMC), a “perturbed observation” 3-dimensional variational assimilation (3D-Var) approach is used (Houtekamer et al. 1996).

Understanding the relative merits of each approach has proved difficult since each forecast center uses a different forecast model, different data assimilation approaches, and even somewhat different sets of observations. Few comparisons have been performed to test the different perturbation methods with the same analysis system, forecast model, and observations. Houtekamer and Derome (1995) compared the skill of the mean forecasts from singular vector, bred, and perturbed observation ensembles using a T21 L3 quasigeostrophic model. Anderson (1996, 1997) provided some comparisons of different approaches using the 3-dimensional Lorenz (1963) model. Hamill et al. (2000) provided a comparison of singular vector, bred, and perturbed observation

methods in a quasi-geostrophic channel model with  $O(10^5)$  degrees of freedom under perfect-model assumptions.

Since all of the operational methods that are currently utilized are approximations of various degrees, some theoretical guidance on what ideally should be used would be helpful. Under assumptions of linearity of error growth and normality of errors, Ehrendorfer and Tribbia (1997) demonstrate that forecast-error covariances for a specified lead time can be predicted most efficiently using an ensemble constructed in the subspace of the leading *analysis-error covariance singular vectors* (AEC SVs). These are the structures that explain the greatest forecast variance and whose initial size is consistent with the analysis-error covariance statistics.

Because of the cost and difficulty of generating such AEC SVs, ECMWF has used a surrogate approach. Their ensemble of initial conditions are constructed to lie in a subspace of the leading initial-time *total-energy singular vectors* (TE SVs). Perturbations evolved from these singular vectors are designed to maximize forecast error variance at 48 h measured in a total-energy norm, subject to the constraint that the initial size of the perturbation is fixed and again measured in a total-energy norm. Unfortunately, the structure of the initial-time TE SVs do not appear to be consistent even with the time-averaged analysis error statistics, i.e., they are not sampling the analysis errors as required by the Liouville equation. For example, Hollingsworth and Lönnerberg (1986) showed that time-averaged background errors (and thus, presumably analysis errors) are largest near the tropopause and much smaller in the middle troposphere, whereas the leading initial-time TE SV perturbation typically is largest in the middle troposphere.

Because of such discrepancies, Barkmeijer et al. (1998, 1999) explored an alternative singular vector calculation, dubbed “Hessian SVs.” The initial-time Hessian SVs are consistent with the analysis-error statistics used in 3D-Var. These error statistics are stationary except to the extent that the observation network varies with time. In their studies, they compared the structure of the initial perturbations and the accuracy of subsequent probabilistic forecasts against those from TE SVs. The leading initial-time Hessian SVs were larger in scale than corresponding initial-time TE SVs, and their amplitude both at the initial time and optimization time was

largest near the tropopause. Hessian SVs typically grew somewhat slower than TE SVs. The Hessian SVs had smaller initial amplitudes over data-rich continents and larger amplitudes over the oceans, consistent with the analysis-error statistics. Though the Hessian SVs had some desirable characteristics, probabilistic forecasts from TE SVs were found to be slightly more skillful. The exact reasons for this were unclear; Barkmeijer et al. hypothesized that perhaps the broad and deep correlation functions in the background-error covariance model used in 3D-Var unrealistically de-emphasized synoptic scales and that with a more realistic error covariance, the Hessian SV structures might more closely resemble those from TE SVs. Gelaro et al. (2002) recently performed a study of singular vectors using an analysis-error *variance* (not covariance) norm and found structures that were somewhat more similar to TE SVs than in the Barkmeijer et al. studies.

To date, no study has documented the structure of flow-dependent AEC SVs. We now have the tools in place to perform this comparison with only minor approximation. The emergence of ensemble-based data assimilation schemes (see, e.g., Evensen 1994, Houtekamer and Mitchell 1998, 2001, Burgers et al. 1998, Hamill et al. 2001, Whitaker and Hamill 2002) provide a vehicle for quantitatively exploring some of these questions. These methods are based on an ensemble of parallel data assimilation cycles. Background-error covariances used during the data assimilation are modeled from the collection of ensemble forecasts. If care is taken to avoid filter divergence (see Hamill et al. 2001 and references therein), this ensemble of initial conditions should sample the distribution of analysis errors.

Such an ensemble offers a hope of answering some interesting questions. For example, using this ensemble, one can readily determine a few leading AEC SVs. This is performed by finding the forecast structures in the space spanned by the ensemble that account for the most error variance. Under assumptions of linearity, the same linear combination of ensemble members that produces an optimal forecast structure can be applied to the ensemble of analyses to indicate the initial-time structure that gave rise to this, producing the initial-time AEC SV. Attraction

tively, this computation can be done without use of the linear tangent and adjoint of the forecast model.

This paper will focus on a description of the structure of these AEC SVs and a comparison with TE SVs as described in earlier studies. We also hope to tangentially inform a debate on adaptive observation strategies. Several recent papers (e.g., Palmer et al. 1998, Gelaro et al. 1999) have suggested that, consistent with the TE SV structure, the most logical levels at which to introduce adaptive observations is in the middle to lower troposphere. Conclusions about the best locations for adaptive observations may be different if the structure of flow-dependent AEC SVs are inconsistent with that from TE SVs.

The paper is organized as follows. Section 2 provides a brief description of the forecast model and the ensemble data assimilation methodology. Section 3 describes the methodology for generating flow-dependent AEC SVs. The details of our experiment and test methodology are described in Section 4. Section 5 describes the characteristics of analysis errors, while section 6 provides results and section 7 the conclusions.

## 2. ENSEMBLE-BASED DATA ASSIMILATION METHODOLOGY

### *a. Forecast Model*

A T31 L15 dry, primitive equation spectral model will be used in the following experiments. There are no terrain features nor surface variations. The model has 22,816 degrees of freedom. The prognostic variables are vorticity, divergence, temperature, and surface pressure. Except for a minor modification to the forcing, described below, the model is essentially equivalent to the model of Held and Suarez (1994).

The experiment is conducted under perfect-model assumptions; that is, the same forecast model is used to generate both a synthetic true state and in the conduct of the ensemble forecasts. To generate a time series of the true state, we started with a random perturbation superimposed upon a resting state. The model is then integrated for 280 days. The first 100 days were discarded, and the remaining 180 days comprise the time series of the true state used in this ex-

periment. Hereafter, day 100 is considered the starting point, the day 0 for all further experiments.

As described in Hamill et al. (2002), our initial experiments with this model using the classical Held and Suarez (1994) forcing frequently produced low-quality analyses in the tropical upper troposphere. After much examination, we concluded that the root cause were small-scale wave motions excited under adiabatic or superadiabatic conditions. We tested the use of linear vertical diffusion to control this noise, but this was largely ineffective. As noted by Bénard et al. (2000), nonlinear vertical diffusion schemes are preferable but must be coded very carefully to ensure stability. We decided as a workaround instead to modify the radiative equilibrium state to which temperature is relaxed, making it slightly more stable in the tropical upper troposphere. The classical Held and Suarez equilibrium state is defined by

$$T_{eq} = \max \left\{ 200K, \left[ 315K - (\Delta T)_y \sin^2 \phi - (\Delta \theta)_z \log \left( \frac{p}{p_0} \right) \cos^2 \phi \right] \left( \frac{p}{p_0} \right)^\kappa \right\} \quad (1)$$

where  $(\Delta T)_y = 60$  K,  $\phi$  is the latitude,  $(\Delta \theta)_z = 10$  K,  $p_0 = 1000$  hPa, and  $\kappa = R/c_p = 2/7$ , and  $c_p = 1004$  J kg<sup>-1</sup> K<sup>-1</sup>. Our modified Held-Suarez forcing is of the form

$$T_{eq} = \max \left\{ 200K, \left[ 315K - (\Delta T)_y \sin^2 \phi - (\Delta \theta)_z \log \left( \frac{p}{p_0} \right) (1 + \cos^2 \phi) \right] \left( \frac{p}{p_0} \right)^\kappa \right\} \quad (2)$$

The change in the equilibrium state between the two is illustrated in Fig. 1.

#### *b. Ensemble data assimilation methodology*

The assimilation scheme used here has been dubbed the ensemble square-root filter, or “En-SRF.” A complete description of it and the rationale for its use is provided in Whitaker and Hamill (2002). The underlying principle is to run an ensemble of parallel forecast and data assimilation cycles, ensuring that the ensemble mean analysis and the analysis-error covariance as estimated by the ensemble are consistent with that predicted by Kalman-filter theory.

We follow the notational convention of Ide et al. (1997). Let  $\mathbf{x}^b$  be a background model forecast,  $\mathbf{y}^o$  be a set of observations,  $\mathbf{H}$  be an operator that converts the model state to the obser-



vation space, here assumed linear. Let  $\mathbf{P}^b$  be the background-error covariance matrix, and  $\mathbf{R}$  be the observational-error covariance matrix. The minimum error variance estimate of the analyzed state  $\mathbf{x}^a$  is then given by the traditional Kalman filter update equation (Lorenc 1986),

$$\mathbf{x}^a = \mathbf{x}^b + \mathbf{K}(\mathbf{y}^o - \mathbf{H}\mathbf{x}^b), \quad (3)$$

where

$$\mathbf{K} = \mathbf{P}^b \mathbf{H}^T (\mathbf{H} \mathbf{P}^b \mathbf{H}^T + \mathbf{R})^{-1}. \quad (4)$$

The expected analysis-error covariance is

$$\mathbf{P}^a = (\mathbf{I} - \mathbf{K}\mathbf{H})\mathbf{P}^b. \quad (5)$$

In the standard ensemble Kalman filter (EnKF; Evensen 1994, Houtekamer and Mitchell 1998, Burgers et al. 1998, Hamill et al. 2001), parallel data assimilation cycles are conducted, each cycle updating a member background forecast to a set of perturbed observations perturbed with noise consistent with observational errors.  $\mathbf{P}^b$  is approximated using the sample covariance from an ensemble of model forecasts;  $\mathbf{P}^b = \langle \mathbf{x}'^b \mathbf{x}'^{bT} \rangle$ , where primes denote the deviation from the ensemble mean and  $\langle \cdot \rangle$  denotes the expected value, here computed from the ensemble. In actuality, there is no need to compute and store the full matrix  $\mathbf{P}^b$ . Instead, matrices  $\mathbf{P}^b \mathbf{H}^T$  and  $\mathbf{H} \mathbf{P}^b \mathbf{H}^T$  are estimated directly using the ensemble (Evensen 1994, Houtekamer and Mitchell 1998).

The EnSRF operates similarly, conducting a set of parallel data assimilation cycles. It is convenient in the EnSRF to update the equations for the ensemble mean (denoted by an overbar) and the deviation from the mean separately:

$$\bar{\mathbf{x}}^a = \bar{\mathbf{x}}^b + \mathbf{K}(\mathbf{y}^o - \mathbf{H}\bar{\mathbf{x}}^b), \quad (6)$$

$$\mathbf{x}'^a = (\mathbf{I} - \tilde{\mathbf{K}}\mathbf{H})\mathbf{x}'^b. \quad (7)$$

Here,  $\mathbf{K}$  is the traditional Kalman gain given by Eq. (4), and  $\tilde{\mathbf{K}}$  is the “reduced” gain used to update deviations from the ensemble mean.

When sequentially processing independent observations,  $\mathbf{K}$ ,  $\tilde{\mathbf{K}}$ ,  $\mathbf{H}\mathbf{P}^b$  and  $\mathbf{P}^b\mathbf{H}^T$  are all vectors with the same length as the model state vector, and  $\mathbf{H}\mathbf{P}^b\mathbf{H}^T$  and  $\mathbf{R}$  are scalars. Thus, as first noted by Potter (1964), when observations are processed one at a time,

$$\tilde{\mathbf{K}} = \left( 1 + \sqrt{\frac{\mathbf{R}}{\mathbf{H}\mathbf{P}^b\mathbf{H}^T + \mathbf{R}}} \right)^{-1} \mathbf{K}. \quad (8)$$

The quantity multiplying  $\mathbf{K}$  in Eq. (11) is thus a scalar between 0 and 1. This means that, in order to obtain the desired analysis-error covariance, one uses a modified Kalman gain to update deviations from the ensemble mean that is reduced in magnitude relative to the traditional Kalman gain. Thus, deviations from the mean are reduced less in the analysis using  $\tilde{\mathbf{K}}$  than they would be using  $\mathbf{K}$ . In the EnKF, the excess variance reduction caused by using  $\mathbf{K}$  to update deviations from the mean is compensated for by the introduction of noise to the observations. In the EnSRF, the mean and departures from the mean are updated independently according to Eqs. (6) and (7). If observations are processed one at a time, the EnSRF requires about the same computation as the traditional EnKF with perturbed observations.

The general analysis methodology is thus as follows: generate a set of perturbed initial conditions. Make  $n$  forecasts forward to the next data assimilation time. Perform  $n + 1$  parallel data assimilation cycles, updating the mean state using (6) and the  $n$  perturbations using (7) and (8). Repeat the process. In each data assimilation cycle, observations are assimilated serially.

Some additional algorithmic complexity will be used in order to model background-error covariances more accurately. These include the inflation and localization of covariances. Deviations of perturbations of each member from the ensemble mean are inflated by a small amount before the start of each data assimilation cycle in order to ensure that covariances are not systematically underestimated. Such underestimation can cause a problem known as filter divergence, whereby the influence of new observations is ignored. Covariance localization multiplies the ensemble estimate of covariances with an isotropic function which monotonically decreases with greater distance from the observation. See Hamill et al. (2001) and references therein for an in-depth rationale and mathematical formalism.

### 3. ANALYSIS-ERROR COVARIANCE SINGULAR VECTORS USING ENSEMBLES

Before describing how the leading AEC SVs can be approximated given an ensemble of analyses from the EnKF, we first briefly review the definition and some properties of the AEC SVs. We use the following notational conventions.  $\mathbf{S}$  denotes a symmetric, nonnegative matrix defining a norm for the forecast errors by  $|\mathbf{x}| = \mathbf{x}^T \mathbf{S} \mathbf{x}$ . In what follows, we will define  $|\cdot|$  to be the total energy norm and write  $\mathbf{S} = \mathbf{D} \mathbf{D}^T$ , where  $\mathbf{D}$  is a matrix that transforms and scales the state vector so that  $(\mathbf{D} \mathbf{x})^T \mathbf{D} \mathbf{x}$  is the total energy of  $\mathbf{x}$ .  $\mathbf{M} = \mathbf{M}(t_1, t_2)$  will denote the resolvent of the tangent linear dynamics over the interval  $[t_1, t_2]$  (that is,  $\mathbf{M}$  maps sufficiently small analysis error at  $t = t_1$  onto forecast errors at  $t = t_2$ ).

To find analysis-error covariance singular vectors, we would like to maximize forecast perturbation  $\mathbf{x}'^f$ , measured in a total-energy norm, subject to the constraint that the initial perturbations  $\mathbf{x}'^a$  are sized to be consistent with the analysis-error statistics, i.e.,

$$\max \frac{\mathbf{x}'^f{}^T \mathbf{S} \mathbf{x}'^f}{\mathbf{x}'^a{}^T \mathbf{P}^a \mathbf{x}'^a}$$

or

$$\max \frac{\mathbf{x}'^a{}^T \mathbf{M}^T \mathbf{S} \mathbf{M} \mathbf{x}'^a}{\mathbf{x}'^a{}^T \mathbf{P}^a \mathbf{x}'^a}.$$

The normalization in the denominator ensures that the size and structure of  $\mathbf{x}'^a$  are consistent with those of a perturbation drawn from a normal distribution with zero mean and covariance  $\mathbf{P}^a$ . Thus, when the denominator is large, the error is unlikely. By Rayleigh's principle, these AEC SVs are also a solution to the generalized eigenvalue problem

$$\mathbf{M}^T \mathbf{S} \mathbf{M} \mathbf{u} = \lambda \mathbf{P}^a \mathbf{u} \quad (9)$$

where  $\mathbf{u}$  denotes an eigenvector and  $\lambda$  the associated eigenvalue (also see Barkmeijer et al. 1998).

The significance of the solutions  $\mathbf{u}$  in (9) can be seen by defining  $\mathbf{v} = \mathbf{D} \mathbf{M} \mathbf{u}$ . Multiplying (9) on the left by  $\mathbf{D} \mathbf{M}^T \mathbf{P}^a$  and recalling that  $\mathbf{S} = \mathbf{D} \mathbf{D}^T$  then yields

$$\mathbf{D} \mathbf{M}^T \mathbf{P}^a \mathbf{M} \mathbf{D}^T \mathbf{v} = \lambda \mathbf{v}. \quad (10)$$

The forecast error covariance at the optimization time is  $\mathbf{P}^f = \langle \mathbf{x}'^f \mathbf{x}'^f{}^T \rangle$ . If analysis errors evolve linearly, then  $\mathbf{P}^f = \mathbf{M}\mathbf{P}^a\mathbf{M}^T$  and (10) becomes

$$\mathbf{D}\mathbf{P}^f\mathbf{D}^T\mathbf{v} = \lambda\mathbf{v}. \quad (11)$$

Thus, the solutions  $\mathbf{v}$  of (10) are the eigenvectors of the forecast-error covariance matrix (after transforming and scaling the state with  $\mathbf{D}$ ), and  $\mathbf{u}$  in (9) is the initial error that evolves to produce  $\mathbf{v}$ , via  $\mathbf{v} = \mathbf{D}\mathbf{M}\mathbf{u}$ . We will refer to  $\mathbf{u}$  as the initial-time AEC SV, since it corresponds to an error in the analysis, and to  $\mathbf{v}$  as the evolved or forecast AEC SV, since it corresponds to the forecast error produced by the analysis error  $\mathbf{u}$ .

Now, we wish to approximate the leading AEC SVs using an ensemble of analyses at  $t = t_1$  from the EnSRF and an ensemble of forecasts to  $t = t_2$  initialized from those analyses. Let  $\mathbf{X}_a = (n-1)^{-1/2}[\mathbf{x}_1^a - \bar{\mathbf{x}}^a, \dots, \mathbf{x}_n^a - \bar{\mathbf{x}}^a]$ , where the  $i$ th column vector represents the  $i$ th member  $\mathbf{x}_i^a$ 's analyzed model state deviation from the ensemble mean analysis  $\bar{\mathbf{x}}^a$ . Similarly, let  $\mathbf{X}_f = (n-1)^{-1/2}[\mathbf{x}_1^f - \bar{\mathbf{x}}^f, \dots, \mathbf{x}_n^f - \bar{\mathbf{x}}^f]$ , where  $\mathbf{x}_i^f$  is the forecast from  $\mathbf{x}_i^a$  based on the full (nonlinear) forecast model. In order to approximate the AEC SVs, the ensemble to be used must satisfy

$$\lim_{n \rightarrow \infty} \mathbf{X}_a \mathbf{X}_a^T = \mathbf{P}^a \quad \text{and} \quad \lim_{n \rightarrow \infty} \mathbf{X}_f \mathbf{X}_f^T = \mathbf{P}^f; \quad (12)$$

that is, the sample covariance matrices based on the analysis and forecast ensembles must approximate  $\mathbf{P}^a$  and  $\mathbf{P}^f$ , respectively, for sufficiently large ensembles.

The forecast AEC SVs can be approximated by the solutions of

$$\mathbf{D}\mathbf{X}_f(\mathbf{D}\mathbf{X}_f)^T\mathbf{v} = \lambda\mathbf{v}, \quad (13)$$

This is because, given the second condition in (12), eqns (11) and (13) become identical for large  $n$ . We compute solutions of (13) by representing  $\mathbf{v}$  as a linear combination of the  $n$  forecast deviations, that is,

$$\mathbf{v} = \mathbf{D}\mathbf{X}_f\mathbf{a}. \quad (14)$$

Substituting for  $\mathbf{v}$  in (13) and eliminating a factor of  $\mathbf{D}\mathbf{X}_f$  from each side, we obtain an equivalent (for  $\lambda \neq 0$ ) but smaller  $n \times n$  eigenproblem,

$$(\mathbf{D}\mathbf{X}_f)^T\mathbf{D}\mathbf{X}_f\mathbf{a} = \mathbf{X}_f^T\mathbf{S}\mathbf{X}_f\mathbf{a} = \lambda\mathbf{a} \quad (15)$$

whose solutions can be found by convential numerical techniques. Alternatively, one may compute  $\mathbf{v}$  as the left singular vectors in an SVD of  $\mathbf{D}\mathbf{X}_f$ . We have found negligible differences in the resulting numerical solutions.

To approximate the initial-time AEC SVs, we need a similar approximation to the solutions  $\mathbf{u}$  of (9). This requires the assumption that the forecast-error evolution is approximately linear; in that case,  $\mathbf{X}_f = \mathbf{M}\mathbf{X}_a$  and (15) becomes

$$\mathbf{X}_a^T \mathbf{M}^T \mathbf{S} \mathbf{M} \mathbf{X}_a \mathbf{a} = \lambda \mathbf{a}. \quad (16)$$

Multiplying by  $\mathbf{X}_a$  and setting  $\mathbf{u} = \mathbf{X}_a \mathbf{a}$  then gives, for large  $n$ ,

$$\mathbf{P}^a \mathbf{M}^T \mathbf{S} \mathbf{M} \mathbf{X}_a \mathbf{a} = \mathbf{P}^a \mathbf{M}^T \mathbf{S} \mathbf{M} \mathbf{u} = \lambda \mathbf{u}, \quad (17)$$

which is identical to (9). Note that the leading eigenvectors  $\mathbf{a}$  of (15) provide both an approximate initial AEC SV, through  $\mathbf{u} = \mathbf{X}_a \mathbf{a}$ , and an approximate evolved AEC SV, through  $\mathbf{v} = \mathbf{D}\mathbf{X}_f \mathbf{a}$ , which is exactly (14).

Hence, our overall algorithm for computing the singular vectors from a large ensemble is as follows: (15) is first solved to yield the appropriate linear combination  $\mathbf{a}$ . The initial-time singular vectors are then readily computed as  $\mathbf{u} = \mathbf{X}_a \mathbf{a}$ , and the approximate evolved AEC SVs from  $\mathbf{v} = \mathbf{D}\mathbf{X}_f \mathbf{a}$ . These singular vectors are approximations to the true singular vectors that can only be obtained if the error dynamics are truly linear and if the ensemble size is infinite. In section 6 we will provide some evidence that linear dynamics can appropriately be assumed and that the singular vector structure from ensembles larger than the  $n = 400$  used here should not change much.

#### 4. EXPERIMENTAL DESIGN

Our experiment was conducted over an 180-day period and used a 400-member EnSRF data assimilation system as described in section 2b. In this implementation of the EnSRF, covariances were localized using a Schur product of ensemble covariances with an approximately Gaussian-shaped function with local support (Gaspari and Cohn 1999) reaching a zero value at

7000 km distance from the observation. Before each data assimilation cycle, covariances were inflated by 0.3 %.

Synthetic rawinsondes (raobs) were assimilated every 12 h. The observations consisted of a surface pressure measurement and winds and temperatures at 7 of the sigma levels, located approximately at 900, 766, 633, 500, 366, 233, and 100 hPa. Observations have error characteristics derived from Parrish and Derber (1992); wind errors were assumed to have a standard deviation of 1.73, 2.18, 2.7, 2.8, 3.2, 3.0, and  $2.5 \text{ m s}^{-1}$  respectively at the seven levels, and temperature standard deviations of 1.6, 1.4, 1.3, 1.3, 1.9, 2.5, and  $3.1 \text{ K}$ . Observation errors were assumed uncorrelated in the vertical. Observation locations are shown in Fig. 1; they were chosen to provide a crude analog to the operational raob network, with more observations over the land than the ocean.

Errors are measured in a total energy norm. We follow the definition of total energy from Ehrendorfer and Errico (1995):

$$\| \cdot \| = \sqrt{\frac{1}{2} \int_D \int_0^1 \left[ u^2 + v^2 + \frac{c_p}{T_r} T^2 + R_d T_r \left( \frac{p_s}{p_r} \right)^2 \right] d\sigma dD} \quad (18)$$

where  $D$  indicates the horizontal domain,  $T_r$  is a reference temperature (here, 300 K),  $R_d$  is the gas constant for dry air ( $287 \text{ J K}^{-1} \text{ kg}^{-1}$ ), and  $c_p$  is the specific heat of dry air at constant pressure ( $1004 \text{ J K}^{-1} \text{ kg}^{-1}$ ),  $p_s$  is the surface pressure, and  $p_r$  is a reference pressure (1000 hPa).

In order to examine the structure of singular vectors, we periodically make an ensemble of 400 48-h forecasts from the 400 analyses. The first of these forecasts were conducted from the analyses on day 17.5, and another sample was generated every 5 days thereafter, yielding a total of 33 cases. The AEC SVs were computed using Northern Hemisphere ensemble forecast data north of  $20^\circ \text{ N}$ , and the set of evolved singular vectors were constructed to be orthogonal in a total-energy norm using the methodology outlined in section 3. The evolved singular values and singular vectors were ordered from largest to smallest. To determine the associated initial-time structure, the linear combination of ensemble forecast members that produced a given evolved singular vector is used, but applied to the initial-time ensemble. Under linearity assumptions,

this should produce the correct initial-time structure. The extent to which this assumption is valid will be examined in the section 6.

## 5. ANALYSIS ERROR CHARACTERISTICS

Before examining the structure of the AEC SVs, we first document the characteristics of analysis errors, which are crucial in determining that structure. A time series of the domain-average ensemble mean analysis error is shown in Fig. 3. Errors decreased quickly and decreased to a very low value, punctuated by occasional spikes of somewhat higher error. Figure 4 a-b shows a zonal-mean cross section of the Northern Hemisphere ensemble mean analysis error. Wind errors were largest at the tropopause, with distinct maxima at three locations, near the equator, in the subtropical jet core, and near the North Pole. The former was primarily due to small-scale wave motions generated when the atmosphere is adiabatic or superadiabatic; this maximum would have been substantially larger without the use of the modified Held-Suarez forcing discussed in section 2a. The maximum in the midlatitudes was due to rapid error growth associated with the subtropical jet, and the maximum at the pole is due to a lack of observations. Temperature errors had a less complex structure, with a tropospheric maximum near the pole and a minimum in the tropical lower troposphere. Though we will focus on the Northern Hemisphere hereafter, where errors are very small, we note that the errors were generally much larger in the Southern Hemisphere, where the observational network is more sparse (Fig. 5).

One desirable property from an ensemble data assimilation system is that the analyses and the true state should be able to be considered random samples from the same probability distribution. This can be evaluated with rank histograms (Hamill 2001 and references therein). Figure 6 shows selected rank histograms for several analysis variables. With the exception of temperatures in the tropical upper troposphere, the predominant characteristic of the analyses was a slight excess of spread in the ensembles, manifested in a convex shape to the histograms. The apparent bias of tropical upper-tropospheric temperatures was initially a major concern, suggesting a problem such as filter divergence. However, as shown in Fig. 4, the ensemble mean

temperature analysis error in the tropics was exceedingly small. A map of zonally and temporally averaged temperature bias is presented in Fig. 7. The bias was also uniformly small; at 300 hPa in the tropics, the bias is  $\sim 0.10$  K. Since the analysis error of temperatures are typically about 0.2 K or less in the tropics (Fig. 4), this tiny bias has a large effect on the rank histograms. Since our concern will be primarily in the Northern Hemisphere midlatitudes where rank histograms are generally more uniform, we conclude that the ensemble should generally be useful for providing random samples of analysis error.

## 6. RESULTS

### *a. Structure of analysis-error covariance singular vectors*

We first consider the growth rate of the ordered singular vectors, shown in Fig. 8a. Averaged over many cases, the energy of the leading singular vector grew by a factor of slightly less than 4 during the 48-h forecast. Since energy is a squared quantity, this implies that perturbations approximately doubled in size during the 48 h. Though this growth rate may seem small, the error doubling time for this model at this resolution is around 4 days (higher-resolution versions of this model have faster, more realistic error doubling times). Thus, the leading singular vector grew approximately twice as fast as the leading Lyapunov vector.

In this analysis, the singular vectors were ordered by the amount of forecast error variance that they explain. This does not imply that the leading singular vector is necessarily associated with the fastest growing structure. The largest forecast error could be due to rapid error growth, but it may also be due to the initial analysis structure having relatively large errors in that direction in phase space. Such a contingency is illustrated by Fig. 8b, showing the growth rates for an individual case (day 132.5). Here, singular vector 3 grew faster than both singular vectors 1 and 2.

Consider now the average vertical structure of the leading singular vector. Figure 9 a-b illustrates the zonal-mean structure (areally weighted by the cosine of latitude) at the initial time and at the final time (48 h). Amplitudes at both times were maximized near the tropopause, with



a secondary maximum near the surface. This structure is qualitatively unlike that of TE SVs, as discussed in Buizza and Palmer (1995) and Barkmeijer et al. (1998, 1999). The initial-time structure of the leading TE SV had largest amplitudes in the middle- to lower troposphere, around 700 hPa, whereas these AEC SVs have a minimum amplitude at this pressure.

The growth of various components were also examined. When one examines the amplification of individual wind components (not shown), the singular vectors were dominated by the meridional wind component, with much less amplitude in the zonal wind and temperature components. Temperature perturbations were found to grow primarily near the lower boundary, with less growth aloft. When the wind structure was decomposed into rotational and divergent components, nearly all of the energy of the leading singular vector was contained in the rotational component, very little in the divergent component. This indicates that for this model, the most rapidly growing perturbations were essentially balanced. This differs from results of Errico (2000) and Montani and Thorpe (2002), who found a significant ageostrophic component in the initial-time TE SVs.

The typical horizontal structure was also unlike that documented in previous descriptions of TE SVs. Figures 10 a-b shows one case day's AEC SV structure at the initial and final times. The singular vectors were synoptic in scale and had significant projections at most longitudes. Our first thought was that this non-locality might have been a result of the insufficient ensemble size; perhaps 400 members is not enough to converge to a correct, more localized structure. However, visual comparisons of the leading singular vector from 25- and 100-member ensembles suggest that the global nature of the singular vector does not appear to decrease with increasing sample size (Fig. 11). Note, however, that this global structure may well be an artifact of the simplicity of the forecast model, which does not have land/water interfaces or terrain features to displace the storm tracks.

The power spectrum of the leading singular vector (Fig. 12) shows that power was peaked around wavenumber 10 for both the initial-time and the evolved singular vectors. The growth rate of the perturbations was roughly similar at all scales up to wavenumber 25. This, again,

was dramatically different than the TE SVs, which grow from smaller initial scales to larger final scales (e.g., Barkmeijer et al. 1999; Fig. 1).

Snyder et al. (2002) and Hamill et al. (2002) demonstrated that forecast ensembles have the tendency to concentrate variance along gradients in potential vorticity (PV) (see also Thompson 1986 and Fischer et al. 1998). This was true of evolved structures that were initialized to be random and white in total energy. The same characteristic concentration along PV gradients was seen in both the initial-time and evolved structures for perturbations from a perturbed-observation ensemble using 3D-Var for the data assimilation. Is the characteristic concentration along PV gradients replicated in these initial-time AEC SVs? As an example, Fig. 13 shows a sample horizontal cross section of PV and the spread in analysis PV from this model for day 32.5. Large spread of PV was hardly ever associated with weak gradients; the correlation between the gradient of PV and the spread is  $\sim 0.6$ . A zonal and temporal average of the enstrophy (squared PV) for leading initial-time SV is shown in Fig. 14. The average PV of the leading singular vector at 500 hPa in the middle-latitudes is at the largest  $\sim 1/10$ th its amplitude in the stratosphere; PV variance is concentrated in the stratosphere, just as in the basic state. The typical structure of PV for the leading initial-time TE SV is typically largest in the middle and lower troposphere with little amplitude in the stratosphere.

Another characteristic of TE SVs is for the PV perturbation at the initial-time to be strongly tilted upshear with increasing height (e.g. Montani and Thorpe 2002, Fig. 1). This characteristic is not typically seen in AEC SVs, as shown by the vertical cross section in Fig. 15. Note, however, that a similar vertical cross section of streamfunction for the leading SV did show a characteristic upshear tilt (not shown).

Overall, the evidence provided here consistently suggests that the structure of flow-dependent AEC SVs is markedly different than that of TE SVs.

#### *b. Sampling and linearity issues.*

We have not yet examined some of the underlying assumptions for creating these AEC SVs. There were several possible sources for error in the computation of these AEC SVs. First, though

the ensemble size was large, perhaps the singular vector structure would have been significantly different if the ensemble size were infinite. Second, we assume that errors grew linearly during the forecast. We would like to examine the validity of each of these assumptions.

By examining the structure of the leading singular vector shown in Figs. 10b and 11, one may get the impression that the singular vector structure doesn't change much with ensemble size. Hence, 400 members ought to be enough to estimate them with sufficient accuracy. However, if one examines the leading singular vector structure on other case days, sometimes the structure of the leading singular vector from 25, 100, and 400-member ensembles can appear quite different. Does this indicate a lack of convergence and the need for a yet larger ensemble? If one considers the convergence of the leading singular vector as a standard, then more members may have been needed to achieve convergence. However, of greater consequence for ensemble forecasting is the question of whether the leading singular vectors of small and larger ensembles span the same subspace. If they do, that subspace is converged, and adding additional ensemble members are not required. This aspect can be examined by calculating the *subspace similarity*, finding out how much the singular vectors of a smaller ensemble, for example, project into the subspace of a larger ensemble. Such calculations were also demonstrated in Buizza (1994) and Hamill et al. (2000). Figure 16 shows the subspace similarity of initial-time and evolved singular vectors between ensembles of size 25, 100, and 400. As indicated, the leading 25 initial-time singular vectors from the ensembles of size 25 and 100 projected moderately onto the subspace of the leading 25 singular vectors from the 400-member ensemble (Fig. 16a). The projection was much stronger for the evolved singular vectors (Fig. 16b), where for the first 10 singular vectors of the 100-member ensemble, the projection is greater than 95 percent. This suggests that there is noisiness in the initial time AEC SVs that is somewhat irrelevant to the evolved structure, given a long-enough optimization time. This also indicates that a larger ensemble is required to represent analysis errors than to represent forecast errors (see also Hamill et al. 2002). Barkmeijer et al. (1998, 1999) and others have previously noted that the evolved structure of ensembles tends to be very similar even when the initial ensembles are

started from quite different structures. This similarity is a result of the attraction of all perturbations to the lower-dimensional chaotic attractor.

We examined the issue of linearity using the methodology outlined in Gilmour et al. (2001). They denote a nonlinearity index  $\Theta$  as

$$\Theta = \frac{\|\delta^+(t) + \delta^-(t)\|}{0.5 \{ \|\delta^+(t)\| + \|\delta^-(t)\| \}}. \quad (16)$$

$\|\cdot\|$  here denotes a total energy norm north of 20° N,  $\delta^+(t)$  denotes a positive perturbation, and  $\delta^-(t)$  is a negative perturbation. When growth is linear,  $\Theta = 0$ . To calculate  $\Theta$  here, forecasts were integrated to 48 h from two perturbed initial conditions about the ensemble mean, one in the direction of the leading singular vector, the other its negative pair. Averaged over the 33 cases,  $\Theta$  was very small, typically  $\sim 0.02$ . Of course, as noted above, for a given model  $\Theta$  will depend upon the size of the perturbation and the length of the forecast. Here, the nonlinearity was small both because the initial perturbations were very small and the time scale of the forecast was relatively short compared to the error-doubling time. These results are thus not generalizable to different forecast models with faster error growth rates and larger initial condition errors.

## 7. CONCLUSIONS

We have examined the structure of flow-dependent analysis-error covariance singular vectors (AEC SVs) from a simple general circulation model using an ensemble data assimilation system. This was done in order to understand the singular vector structure when their initial size and structure was constrained to be consistent with analysis error statistics and how this structure may be different than singular vectors using a total-energy initial norm. The structure of these singular vectors has important implications for ensemble forecasting and for ancillary predictability and data assimilation questions such as adaptive observations.

In this experiment, a T31 L15 dry general circulation model was used under perfect-model assumptions. Sets of 400-member ensembles of analyses were generated by an ensemble square-root filter data assimilation system assimilating a sparse network of synthetic radiosonde obser-

uations. Ensembles of 48-h forecasts were also generated from these analyses. The structure of the evolved singular vectors were determined by finding the linear combination of the forecast ensemble members that resulted in the largest forecast-error variance, here measured as a total-energy norm north of 20° N latitude. The same linear combination of analyses specifies the initial-time structure that should evolve to the forecast singular vector under assumptions of linearity of error growth.

The structure of these AEC SVs more closely resembles the structure of Hessian singular vectors than the total-energy singular vectors (TE SVs) currently used by the European Centre for Medium-Range Weather Forecasts to initialize their ensemble forecasts. The AEC SVs computed here had maximum amplitude in mid-latitudes near the tropopause, both at the initial and final times. The AEC SVs were synoptic in scale and, for this model, did not appear to be geographically localized. This contrasts with TE SVs, which started off relatively smaller in scale and had amplitudes typically largest in the lower- to middle troposphere.

The theoretically appropriate choice of initial norm for generating singular vectors perturbations for ensemble forecasts is a *flow-dependent* analysis-error covariance norm such as employed here. To the extent that analysis errors in our simplified model resemble those in global numerical weather prediction models, the difference in structure between these singular vectors and ECMWF's TE SVs suggest that operational ensemble forecasts could be improved; the type of singular vector that are used to generate initial perturbations should be changed to AEC SVs, were this computation practical. The choice of initial norm is likely to be especially important for short-range ensemble forecasts (SREFs), since the structure of forecast perturbations would then reflect more strongly the flow-dependent structure in the initial perturbations. In addition to differences in structure, if TE SVs are used for SREFs, there is likely to be too little spread in short-range ensemble near the surface and near the tropopause, causing such ensembles to be unreliable at short lead times. This is because TE SVs grow more rapidly than AEC SVs and typically use initial amplitudes tuned to produce an appropriate forecast spread at much later times.

The difference between the structure of AEC SVs and TE SVs also has implications for adaptive observing strategies; as noted in the introduction, several sensitivity studies based on total-energy singular vector techniques have suggested that correcting the analysis errors in the middle troposphere should lead to the largest forecast improvement. Since initial-time AEC SVs and analysis errors were largest near the jet level, these results indicate that adaptive observations at jet level ought to have more corrective effect to the analysis and subsequent forecast.

The calculation of AEC SVs in this study was facilitated by the existence of an ensemble-based data assimilation system; none of the major operational weather prediction facilities yet have such a data assimilation system in place, and the relative accuracy of ensemble data assimilation systems relative to 4D-Var is still unknown. Yet there are reasons for the operational centers to give serious consideration to these techniques. In this paper, we showed that analysis errors can be reduced to a remarkably low level with relatively few observations, albeit in a perfect-model simulation with a simple model. The key to this reduction was the flow-dependent background-error covariances generated by the ensemble filter, which produced a more optimal weighting of the background relative to the observations. The dramatically low errors demonstrated here do not seem to be a fluke, either: a growing body of contemporaneous literature has also demonstrated the appeal of ensemble filters for atmospheric, oceanic, and land-surface assimilation problems (Evensen 1994, Evensen and van Leeuwen 1996, Burgers et al. 1998, Houtekamer and Mitchell 1998, 2001, van Leeuwen 1999, Lermusiaux and Robinson 1999, Anderson and Anderson 1999, Hamill and Snyder 2000, Keppenne 2000, Heemink et al. 2000, Hamill et al. 2001, Anderson 2001, Pham 2001, Whitaker and Hamill 2002, Reichle et al. 2002).

The appeal of ensemble filters may be greater yet if one considers the improvements they may foster for ancillary applications. Ensemble filters readily generate sets of initial conditions for ensemble forecasts that are automatically consistent with flow-dependent analysis-error statistics. They may facilitate more accurate computation of where adaptive observations are needed (Hamill and Snyder 2002), for parameter estimation (e.g., Anderson 2001), and for computation of AEC SVs, as demonstrated here.

An issue we have not addressed in this study is the relative value of ensemble forecasts initialized with random perturbations vs. perturbations in the subspace of the singular-vectors. The framework outlined in this paper provides a natural way of performing such tests, and we hope to address this in our future work.

## REFERENCES

- Anderson, J. L., 1996: A method for producing and evaluating probabilistic forecasts from ensemble model integrations. *J. Climate*, **9**, 1518-1530.
- , 1997: Impact of dynamical constraints on the selection of initial conditions for ensemble predictions: low-order perfect model results. *Mon. Wea. Rev.*, **125**, 2969-2983.
- , and S. L. Anderson, 1999: A Monte Carlo implementation of the nonlinear filtering problem to produce ensemble assimilations and forecasts. *Mon. Wea. Rev.*, **127**, 2741-2758.
- , 2001: An ensemble adjustment Kalman filter for data assimilation. *Mon. Wea. Rev.*, **129**, 2884-2903.
- Barkmeijer, J., M. van Gijzen, and F. Bouttier, 1998: Singular vectors and estimates of the analysis error covariance metric. *Quart. J. Roy. Meteor. Soc.*, **124**, 1695-1713.
- , R. Buizza, and T.N. Palmer, 1999: 3D-Var Hessian singular vectors and their potential use in the ECMWF ensemble prediction system. *Quart. J. Roy. Meteor. Soc.*, **125**, 2333-2351.
- Bénard, P., A. Marki, P. N. Neytchev, and M. T. Prtenjak, 2000: Stabilization of nonlinear vertical diffusion schemes in the context of NWP models. *Mon. Wea. Rev.*, **128**, 1937-1948.
- Buizza, R., 1994: Sensitivity of optimal unstable structures. *Quart. J. Roy. Meteor. Soc.*, **120**, 429-451.
- , and T. N. Palmer, 1995: The singular-vector structure of the global atmospheric circulation. *J. Atmos. Sci.*, **52**, 1434-1456.
- Burgers, G., P. J. van Leeuwen, and G. Evensen, 1998: Analysis scheme in the ensemble Kalman filter. *Mon. Wea. Rev.*, **126**, 1719-1724.
- Ehrendorfer, M., 1994: The Liouville equation and its potential usefulness for the prediction of forecast skill. part I: theory. *Mon. Wea. Rev.*, **122**, 703-713.
- , and R. M. Errico, 1995: Mesoscale predictability and the spectrum of optimal perturbations. *J. Atmos. Sci.*, **52**, 3475-3500.



- , and J. J. Tribbia, 1997: Optimal prediction of forecast error covariances through singular vectors. *J. Atmos. Sci.*, **54**, 286–313.
- Errico, R. M., 2000: The dynamical balance of leading singular vectors in a primitive-equation model. *Quart. J. Roy. Meteor. Soc.*, **126**, 1601–1618.
- Evensen, G., 1994: Sequential data assimilation with a nonlinear quasigeostrophic model using Monte Carlo methods to forecast error statistics. *J. Geophys. Res.*, **99 (C5)**, 10143–10162.
- , and P. J. van Leeuwen, 1996: Assimilation of Geosat altimeter data for the Agulhas current using the ensemble Kalman filter with a quasigeostrophic model. *Mon. Wea. Rev.*, **124**, 85–96.
- Fischer, C. A. Joly, and F. Lalaurette, 1998: Error growth and Kalman filtering within an idealized baroclinic flow. *Tellus*, **50A**, 596–615.
- Gaspari, G. and S. E. Cohn, 1999: Construction of correlation functions in two and three dimensions. *Quart. J. Roy. Meteor. Soc.*, **125**, 723–757.
- Gelaro, R., R. H. Langland, G. D. Rohaly, and T. E. Rosmond, 1999: An assessment of the singular vector approach to targeted observing using the FASTEX dataset. *Quart. J. Roy. Meteor. Soc.*, **125**, 3299–3327.
- , T. E. Rosmond, and R. Daley, 2002: Singular vector calculations with an analysis error variance metric. *Mon. Wea. Rev.*, **130**, 1166–1186.
- Gilmour, I., L. A. Smith, and R. Buizza, 2001: Linear regime duration: is 24 hours a long time in synoptic weather forecasting? *J. Atmos. Sci.*, **58**, 3525–3539.
- Hamill, T. M., C. Snyder, and R. E. Morss, 2000: A comparison of probabilistic forecasts from bred, singular vector, and perturbed observation ensembles. *Mon. Wea. Rev.*, **128**, 1835–1851.
- , and ———, 2000: A hybrid ensemble Kalman filter / 3d-variational analysis scheme. *Mon. Wea. Rev.*, **128**, 2905–2919.
- , 2001: Interpretation of rank histograms for verifying ensemble forecasts. *Mon. Wea. Rev.*, **129**, 550–560.

- , J. S. Whitaker, and C. Snyder, 2001: Distance-dependent filtering of background error covariance estimates in an ensemble Kalman filter. *Mon. Wea. Rev.*, **129**, 2776-2790.
- , ———, and ———, 2001: Generating initial conditions for ensemble forecasts: Monte-Carlo vs. dynamic methods. *Preprints, Symposium on Observations, Data Assimilation, and Probabilistic Prediction*. (Orlando) American Meteorological Society, J1-J6.
- , and C. Snyder, 2002: Using improved background error covariances from an ensemble Kalman filter for adaptive observations. *Mon. Wea. Rev.*, **130**, 1552-1572.
- , ———, and R. E. Morss, 2002: Analysis-error statistics of a quasi-geostrophic model using 3-dimensional variational assimilation. *Mon. Wea. Rev.*, accepted. Available at [www.cdc.noaa.gov/~hamill](http://www.cdc.noaa.gov/~hamill).
- Heemink, A. W., M. Verlaan, and A. J. Segers, 2000: Variance-reduced ensemble Kalman filtering. *Mon. Wea. Rev.*, **129**, 1718-1728.
- Held, I. M., and M. J. Suarez, 1994: A proposal for the intercomparison of the dynamical cores of atmospheric general circulation models. *Bull. Amer. Meteor. Soc.*, **75**, 1825-1830.
- Hollingsworth, A., and P. Lönnberg, 1986: The statistical structure of short-range forecast errors as determined from radiosonde data. Part I: the wind field. *Tellus*, **38A**, 111-136.
- Houtekamer, P. L., and J. Derome, 1995: Methods of ensemble prediction. *Mon. Wea. Rev.*, **123**, 2181-2196.
- , L. Lefaivre, and J. Derome, 1996: The RPN ensemble prediction system. *Proc. ECMWF Seminar on Predictability, Vol II*, Reading, United Kingdom, 121-146. [Available from ECMWF, Shinfield Park, Reading, Berkshire RG2 9AX, United Kingdom].
- , and H. L. Mitchell, 1998: Data assimilation using an ensemble Kalman filter technique. *Mon. Wea. Rev.*, **126**, 796-811.
- , and ———, 2001: A sequential ensemble Kalman filter for atmospheric data assimilation. *Mon. Wea. Rev.*, **129**, 123-137.
- Ide, K., P. Courtier, M. Ghil, and A. C. Lorenc, 1997: Unified notation for data assimilation: operational, sequential, and variational. *J. Met. Soc. Japan*, **75** (1B), 181-189.

- Keppenne, C. L., 2000: Data assimilation into a primitive equation model with a parallel ensemble Kalman filter. *Mon. Wea. Rev.*, **128**, 1971-1981.
- Lermusiaux, P. F. J., and A. R. Robinson, 1999: Data assimilation via error subspace statistical estimation. Part 1: theory and schemes. *Mon. Wea. Rev.*, **127**, 1385-1407.
- Lorenc, A. C., 1986: Analysis methods for numerical weather prediction. *Quart. J. Roy. Meteor. Soc.*, **112**, 1177-1194.
- Lorenz, E. N., 1963: Deterministic nonperiodic flow. *J. Atmos. Sci.*, **20**, 131-140.
- Molteni, F., R. Buizza, T. N. Palmer, and T. Petroliaigis, 1996: The ECMWF ensemble prediction system: methodology and validation. *Quart. J. Roy. Meteor. Soc.*, **122**, 73-119.
- Montani, A., and A. J. Thorpe, 2002: Mechanisms leading to singular-vector growth for FAS-TEX cyclones. *Quart. J. Roy. Meteor. Soc.*, **128**, 131-148.
- Palmer, T. N., R. Gelaro, J. Barkmeijer, and R. Buizza, 1998: Singular vectors, metrics, and adaptive observations. *J. Atmos. Sci.*, **55**, 633-653.
- Parrish, D. F., and J. C. Derber, 1992: The National Meteorological Center's Spectral Statistical Interpolation Analysis System. *Mon. Wea. Rev.*, **120**, 1747-1763.
- Pham, D. T., 2001 : Stochastic methods for sequential data assimilation in strongly nonlinear systems. *Mon. Wea. Rev.*, **129**, 1194-1207.
- Potter, J., 1964: W matrix augmentation. M.I.T. Instrumentation Laboratory Memo SGA 5-64, Massachusetts Institute of Technology, Cambridge, MA.
- Reichle, R. H., D. B. McLaughlin, and D. Entekhabi, 2002: Hydrologic data assimilation with the ensemble Kalman filter. *Mon. Wea. Rev.*, **130**, 103-114.
- Snyder, C., T. M. Hamill, and S. J. Trier, 2002: Linear evolution of error covariances in a quasi-geostrophic model. *Mon. Wea. Rev.*, accepted. Available at <http://www.mmm.ucar.edu/individual/snyder/sht.pdf>.
- Thompson, P. D., 1986: A simple approximate method of stochastic-dynamic prediction for small initial errors and short range. *Mon. Wea. Rev.*, **114**, 1709-1715.

- Toth, Z., and E. Kalnay, 1993: Ensemble forecasting at NMC: The generation of perturbations. *Bull. Amer. Meteor. Soc.*, **74**, 2317-2330.
- , and ———, 1997: Ensemble forecasting at NCEP and the breeding method. *Mon. Wea. Rev.*, **125**, 3297-3319.
- van Leeuwen, P.J., 1999: Comment on “Data assimilation using an ensemble Kalman filter technique.” *Mon. Wea. Rev.*, **127**, 1374-1377.
- Whitaker, J. S., and T. M. Hamill, 2002: Ensemble data assimilation without perturbed observations. *Mon. Wea. Rev.*, **130**, 1913-1924. Available from [www.cdc.noaa.gov/~jsw](http://www.cdc.noaa.gov/~jsw).

## FIGURE CAPTIONS

Figure 1. (a) Classical Held and Suarez potential temperature profile; (b) Modified Held and Suarez potential temperature profile (with more stable tropical troposphere) used here. Temperature in Kelvins. Contours are not plotted above 410 K.

Figure 2. Locations of synthetic rawinsonde profiles.

Figure 3. Time series of errors of ensemble mean analysis from ensemble square root filter. Errors are expressed in a total-energy norm integrated over the domain.

Figure 4. Zonal mean of the standard deviation of the ensemble mean analysis error taken from samples between days 35 and 180. (a) Wind error, and (b) temperature error.

Figure 5. Map of time-averaged ensemble mean error in energy norm at 500 hPa. Locations of raobs are overplotted.

Figure 6. Rank histograms of analysis errors. Rank histograms were generated using a subsample of 25 of the 400 ensemble members. Northern Hemisphere rank histograms used samples at every grid point between 30° and 65° N latitude and every 15° longitude. Tropical rank histograms used samples between 15° N and 15° S latitude, and Southern Hemisphere samples between 30° and 65° S latitude.

Figure 7. Zonal average of bias of the ensemble mean analysis. Average was taken from days 35 to 180.

Figure 8. (a) Growth rate (in total energy) as a function of singular vector number. Solid line denotes average over 33 cases, dashed lines the minimum and maximum from the 33 cases. (b) Example of an individual case where growth rates do not monotonically decrease with increasing singular vector number.

Figure 9. Zonal-mean profile of energy of the leading singular vector (weighted by the cosine of latitude). (a) initial time, (b) evolved. Units are  $m^2 s^{-2}$ .

Figure 10. 300 hPa singular vector structure at (a) initial time (here, day 32.5) and (b) final time (here, day 34.5). Heavy solid lines denote streamfunction of true state at that time, and colored lines denote the perturbation to streamfunction from the first singular vector. Contours of true streamfunction are every  $2. \times 10^7 m^2 s^{-1}$ . Streamfunction perturbations in both panels are normalized by the largest perturbation from the forecast, with contours at  $[-0.9, -0.7, \dots, 0.7, 0.9]$ . Red perturbations are positive, blue perturbations negative.

Figure 11. (a) As in Fig. 10b, but from a 100-member ensemble. (b) As in Fig. 10b, but from a 25-member ensemble.

Figure 12. Time- and latitudinally averaged power spectrum of total energy for the leading singular vector. Average is over 33 cases and latitudes from  $35^\circ$  to  $55^\circ$  N latitude. (a) Power spectrum at 300 hPa. (b) Power spectrum at 900 hPa.

Figure 13. Potential vorticity of true state (solid lines) and ensemble standard deviation (dashed lines and shaded) of analysis potential vorticity for  $\theta=310K$  surface on day 32.5. True state PV is contoured at  $[0.5, 1.0, \dots] \times 10^{-7} K Pa^{-1} s^{-1}$  and spread at  $[1.0, 2.0, \dots] \times 10^{-8} K Pa^{-1} s^{-1}$ .

Figure 14. Zonal and time average of enstrophy (squared PV) of leading initial-time AEC SV. Contours are logarithmically plotted. Units are  $K^2 Pa^{-2} s^{-2}$ .

Figure 15. Vertical cross section of PV for the leading AEC SV for the case shown in Figs. 10, 11, and 13. The cross section is around a latitude circle at approximately  $42.5^\circ$  N. Contours are plotted logarithmically; every second contour is one order of magnitude change. Deeper colors denote larger values. (a) Initial-time AEC SV, and (b) evolved AEC SV.

Figure 16. Subspace similarity of leading singular vectors from 25 and 100 member ensemble onto subspace of leading 25 singular vectors from 400-member ensemble. (a) Subspace similarity of initial-time singular vectors. (b) Subspace similarity of evolved singular vectors.

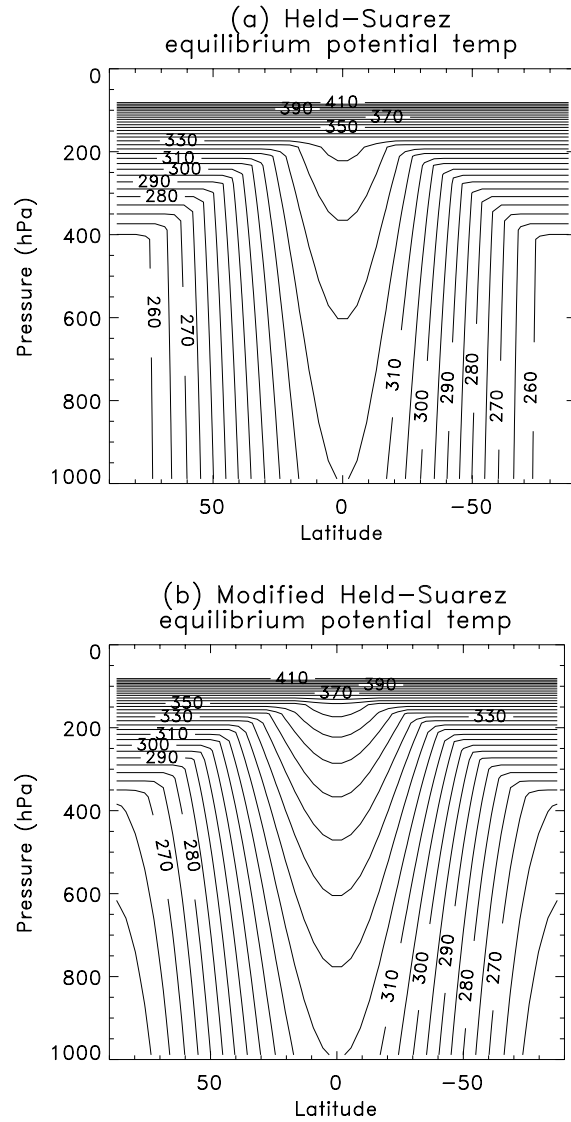


Figure 1. (a) Classical Held and Suarez potential temperature profile; (b) Modified Held and Suarez potential temperature profile (with more stable tropical troposphere) used here. Temperature in Kelvins. Contours are not plotted above 410 K.

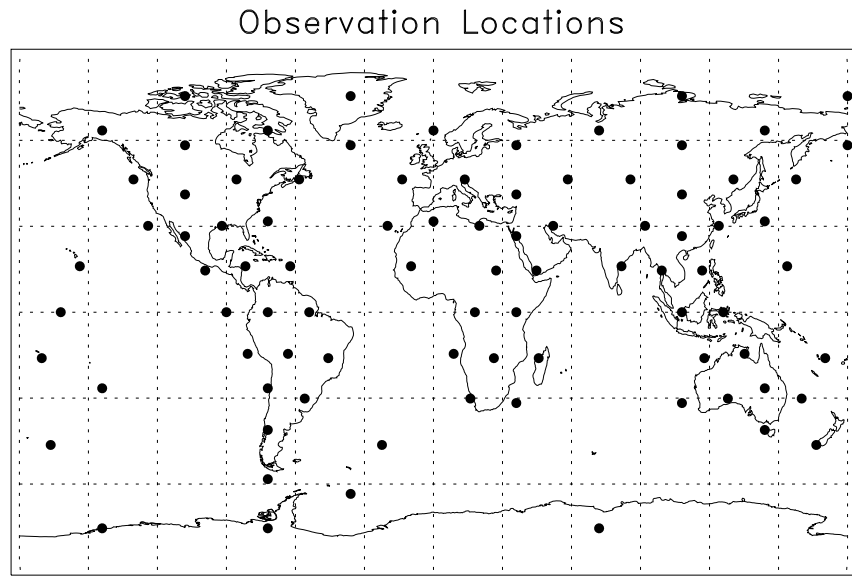


Figure 2. Locations of synthetic rawinsonde profiles.



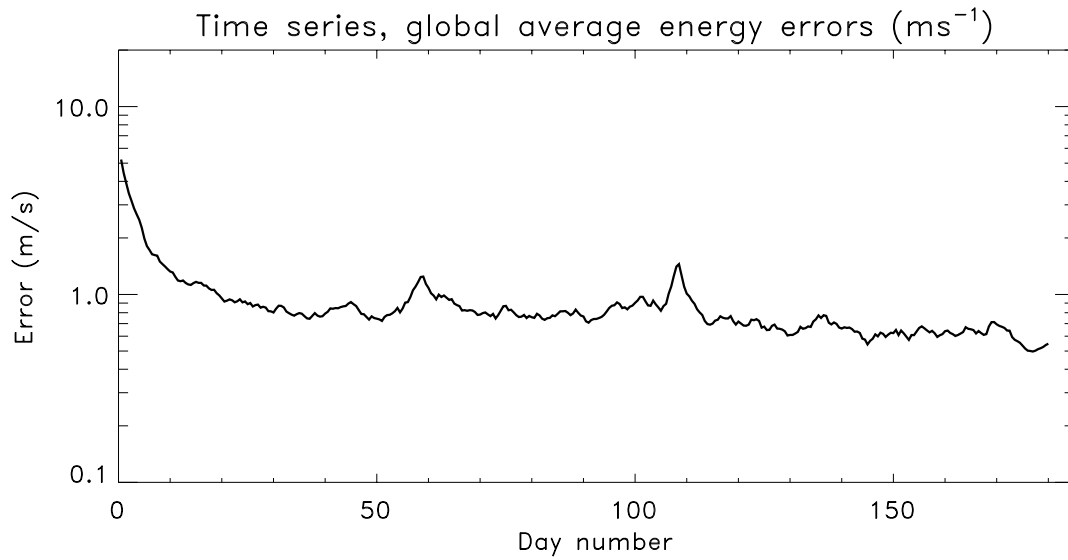


Figure 3. Time series of errors of ensemble mean analysis from ensemble square root filter. Errors are expressed in a total-energy norm integrated over the domain.

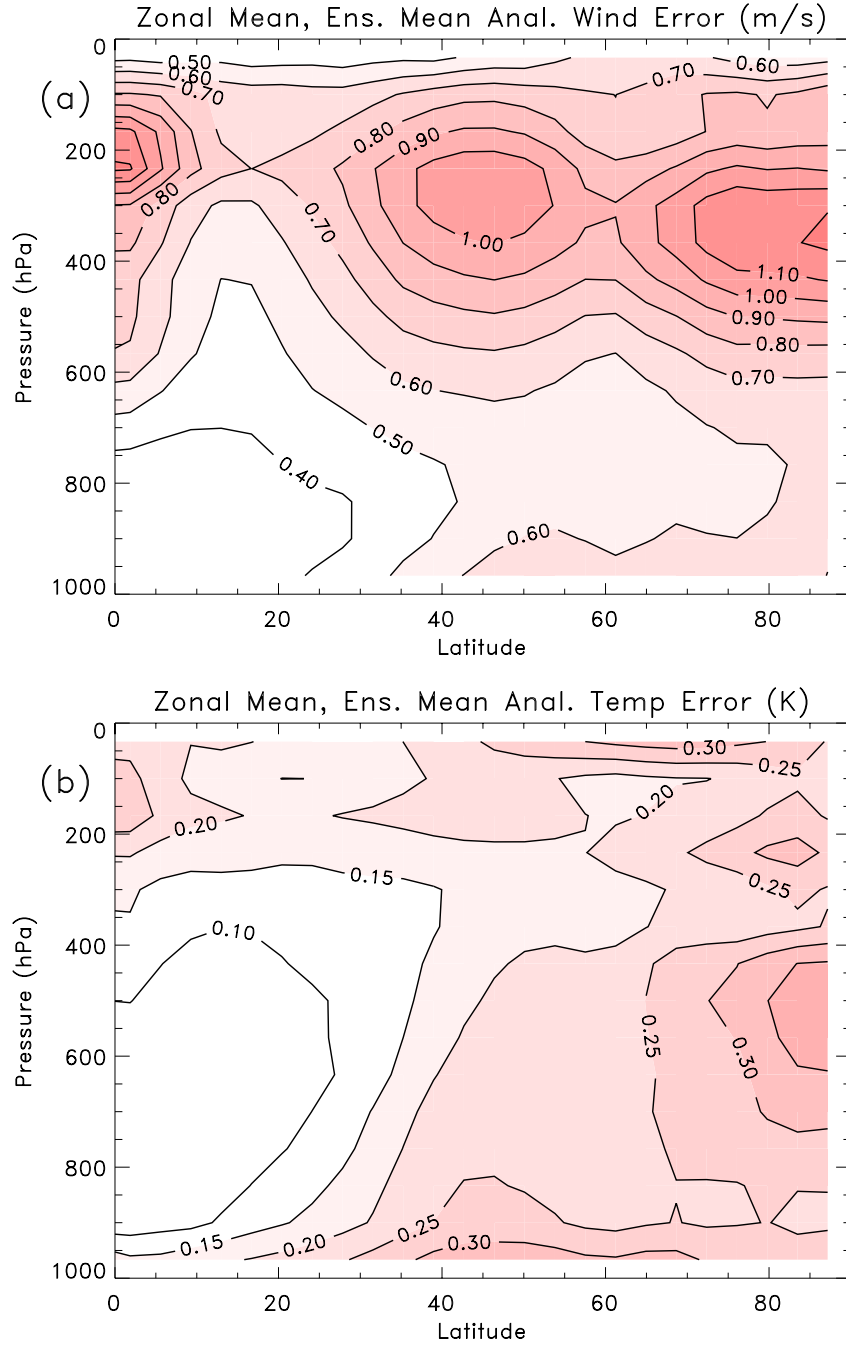


Figure 4. Zonal mean of the standard deviation of the ensemble mean analysis error taken from samples between days 35 and 180. (a) Wind error, and (b) temperature error.

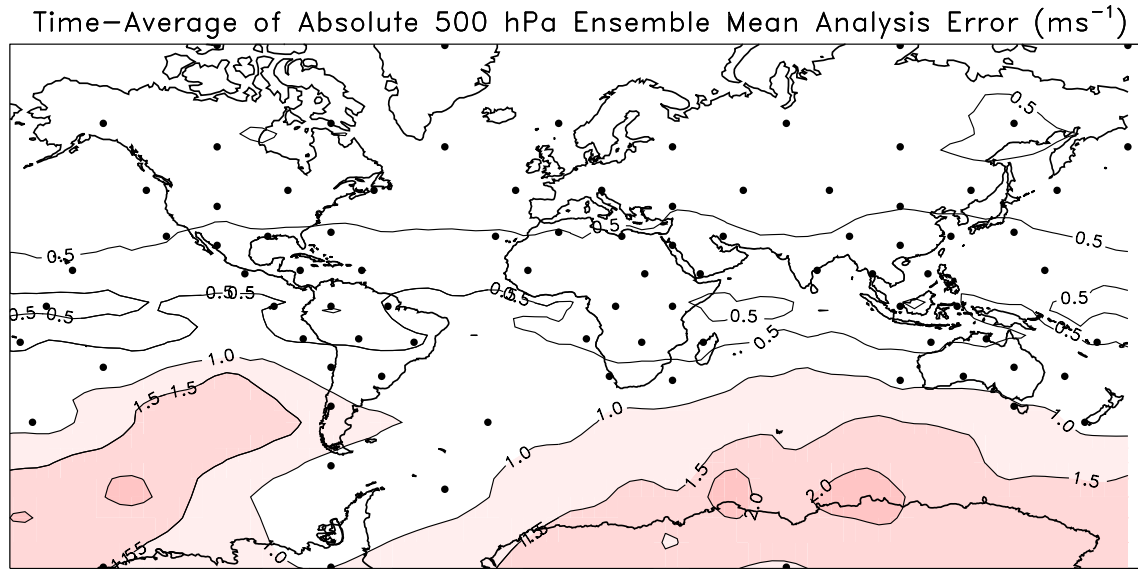


Figure 5. Map of time-averaged ensemble mean error in energy norm at 500 hPa. Locations of raobs are overplotted.

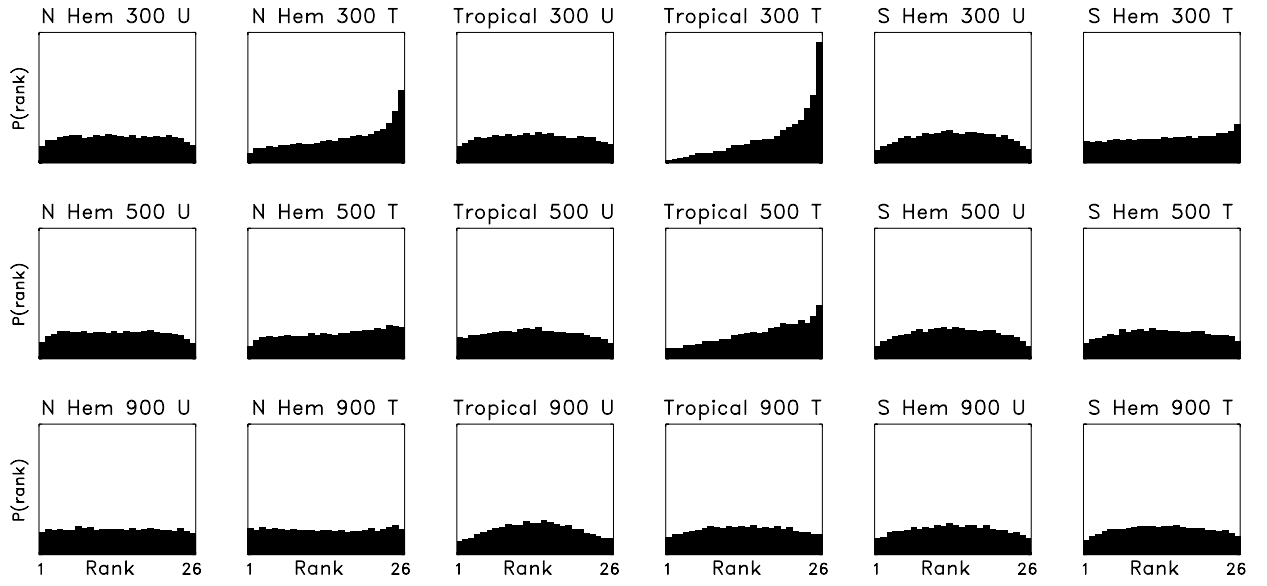


Figure 6. Rank histograms of analysis errors. Rank histograms were generated using a subsample of 25 of the 400 ensemble members. Northern Hemisphere rank histograms used samples at every grid point between  $30^{\circ}$  and  $65^{\circ}$  N latitude and every  $15^{\circ}$  longitude. Tropical rank histograms used samples between  $15^{\circ}$  N and  $15^{\circ}$  S latitude, and Southern Hemisphere samples between  $30^{\circ}$  and  $65^{\circ}$  S latitude.

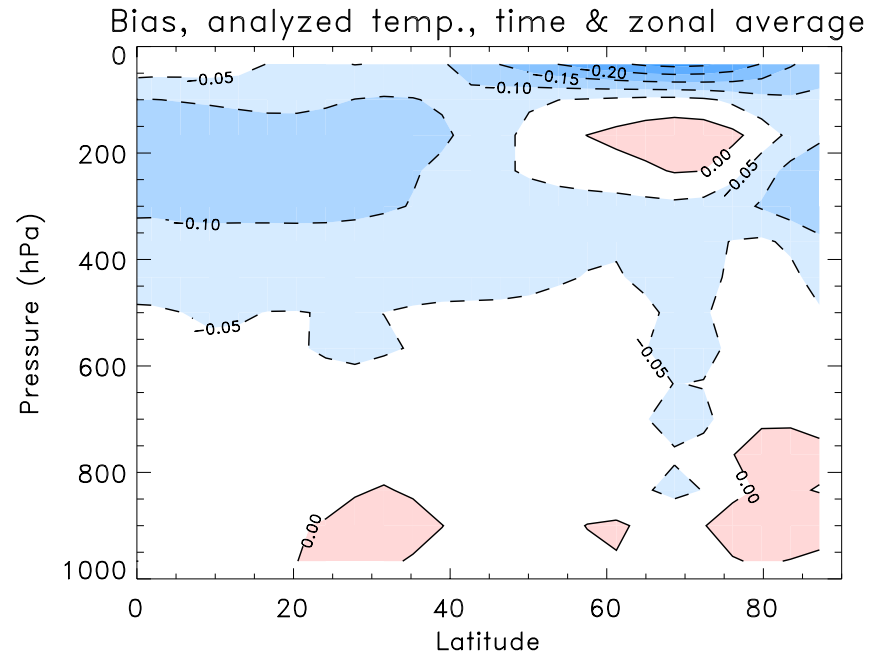


Figure 7. Zonal average of bias of the ensemble mean analysis. Average was taken from days 35 to 180.

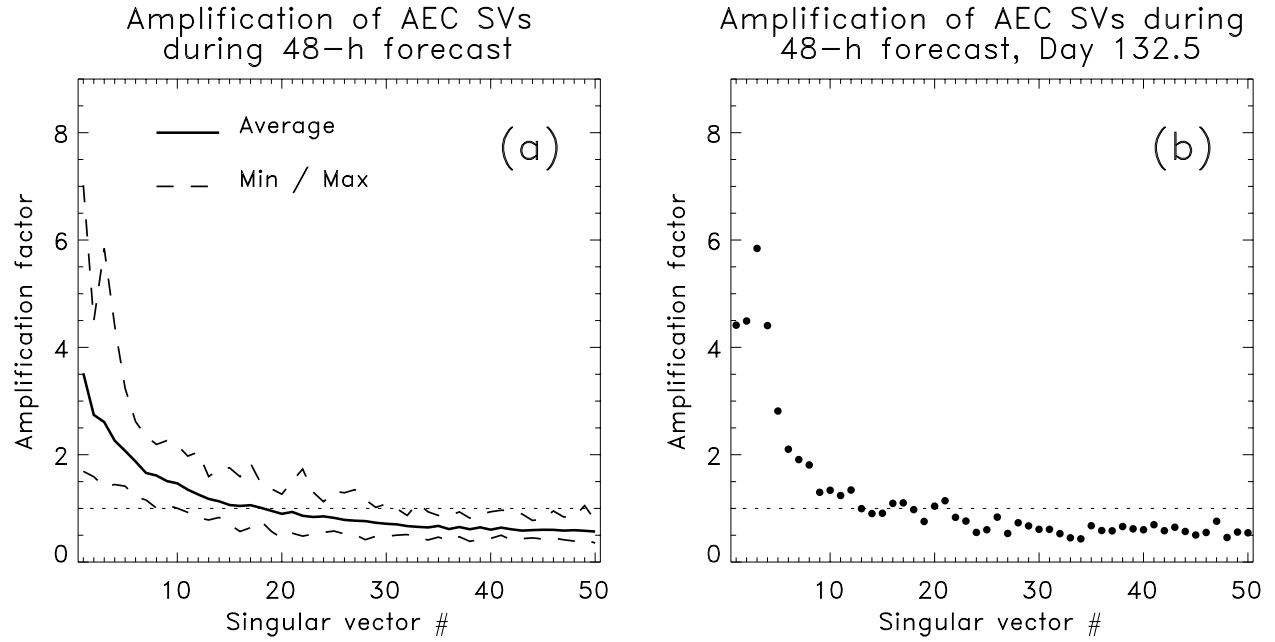


Figure 8. (a) Growth rate (in total energy) as a function of singular vector number. Solid line denotes average over 33 cases, dashed lines the minimum and maximum from the 33 cases. (b) Example of an individual case where growth rates do not monotonically decrease with increasing singular vector number.

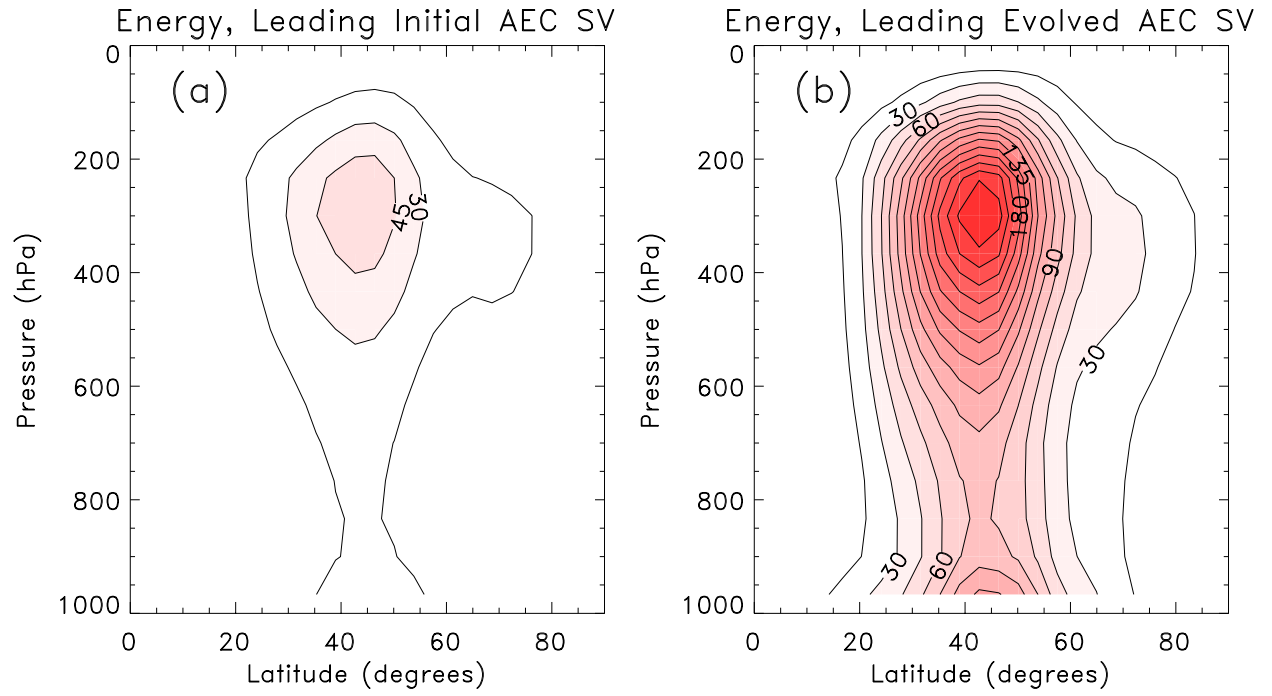


Figure 9. Zonal-mean profile of energy of the leading singular vector (weighted by the cosine of latitude). (a) initial time, (b) evolved. Units are  $m^2 s^{-2}$ .

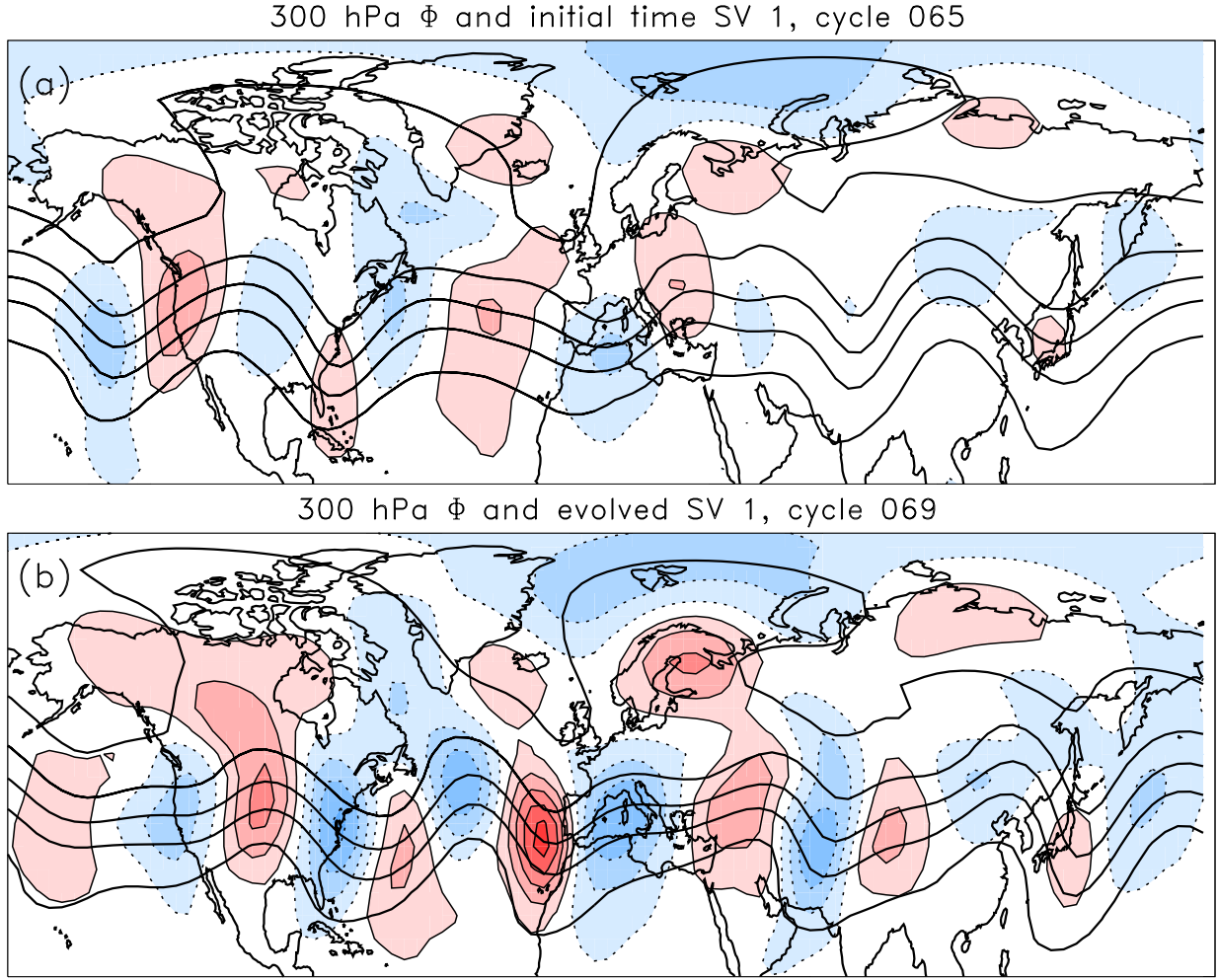
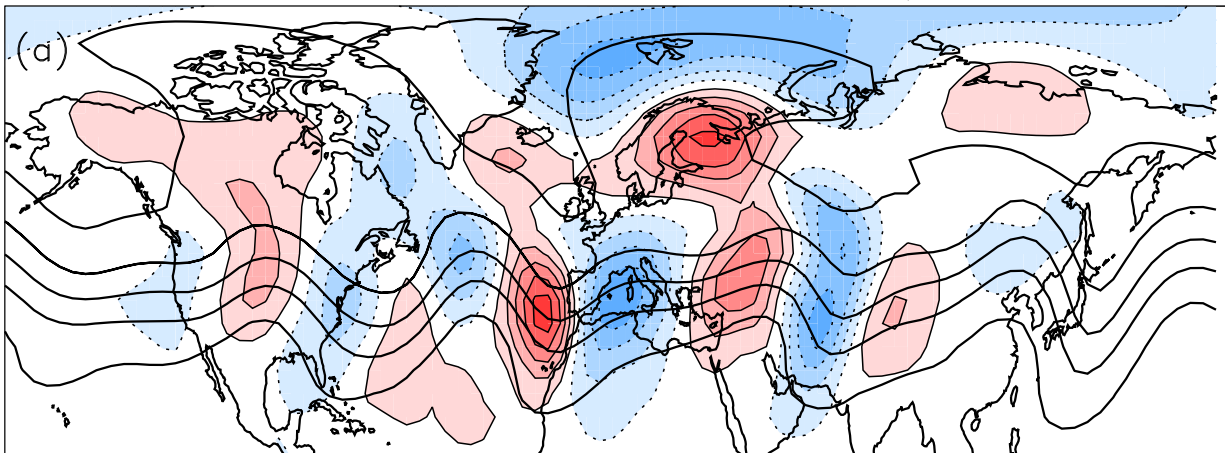


Figure 10. 300 hPa singular vector structure at (a) initial time (here, day 32.5) and (b) final time (here, day 34.5). Heavy solid lines denote streamfunction of true state at that time, and colored lines denote the perturbation to streamfunction from the first singular vector. Contours of true streamfunction are every  $2. \times 10^7 m^2 s^{-1}$ . Streamfunction perturbations in both panels are normalized by the largest perturbation from the forecast, with contours at  $[-0.9, -0.7, \dots, 0.7, 0.9]$ . Red perturbations are positive, blue perturbations negative.



300 hPa  $\Phi$  and evolved SV 1, 100 mbrs, cycle 069



300 hPa  $\Phi$  and evolved SV 1, 25 mbrs, cycle 069

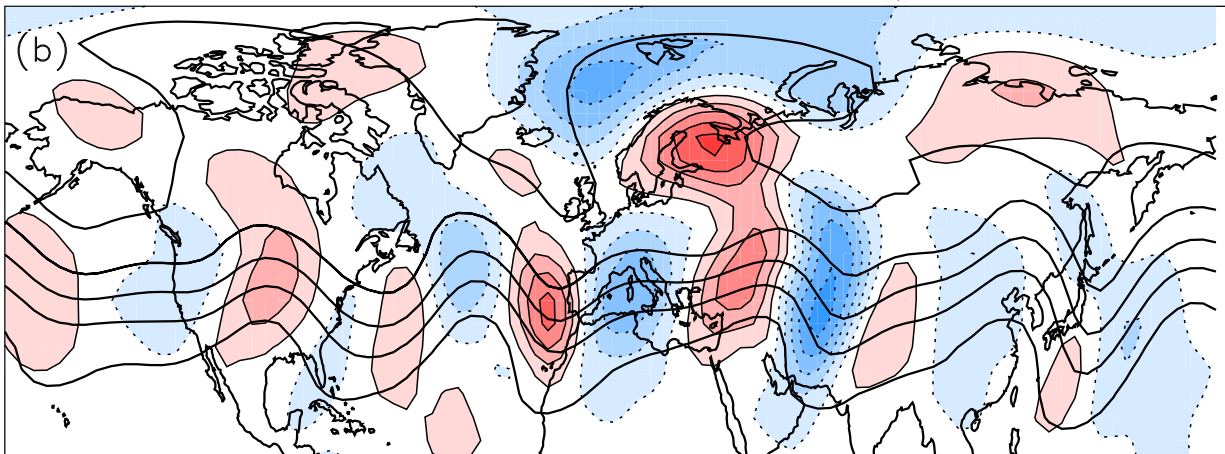


Figure 11. (a) As in Fig. 10b, but from a 100-member ensemble. (b) As in Fig. 10b, but from a 25-member ensemble.

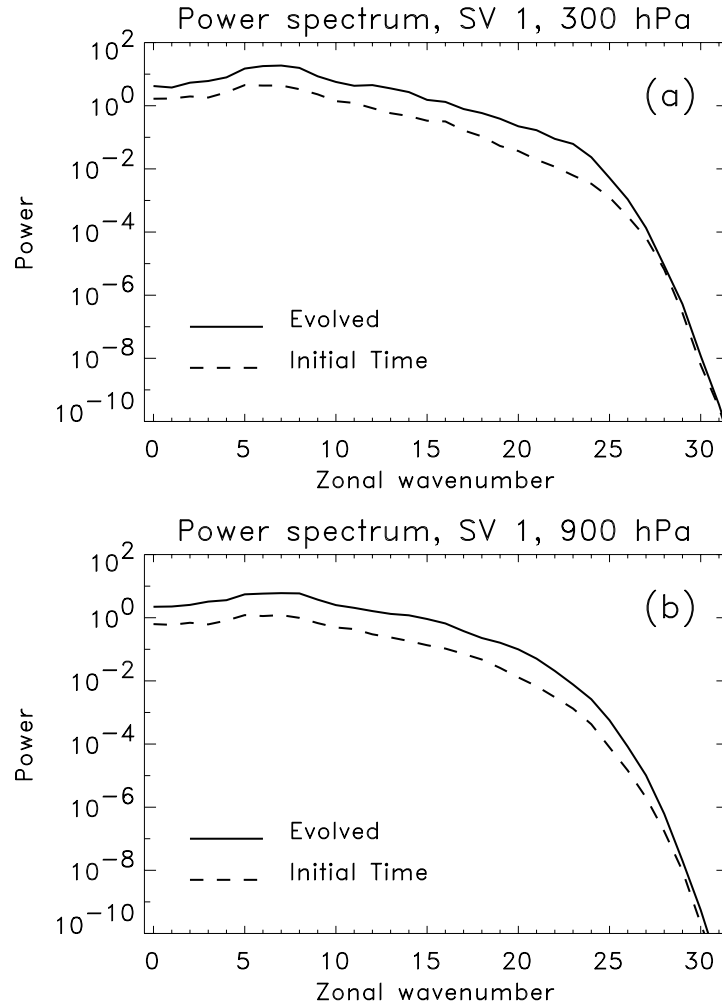


Figure 12. Time- and latitudinally averaged power spectrum of total energy for the leading singular vector. Average is over 33 cases and latitudes from  $35^\circ$  to  $55^\circ$  N latitude. (a) Power spectrum at 300 hPa. (b) Power spectrum at 900 hPa.

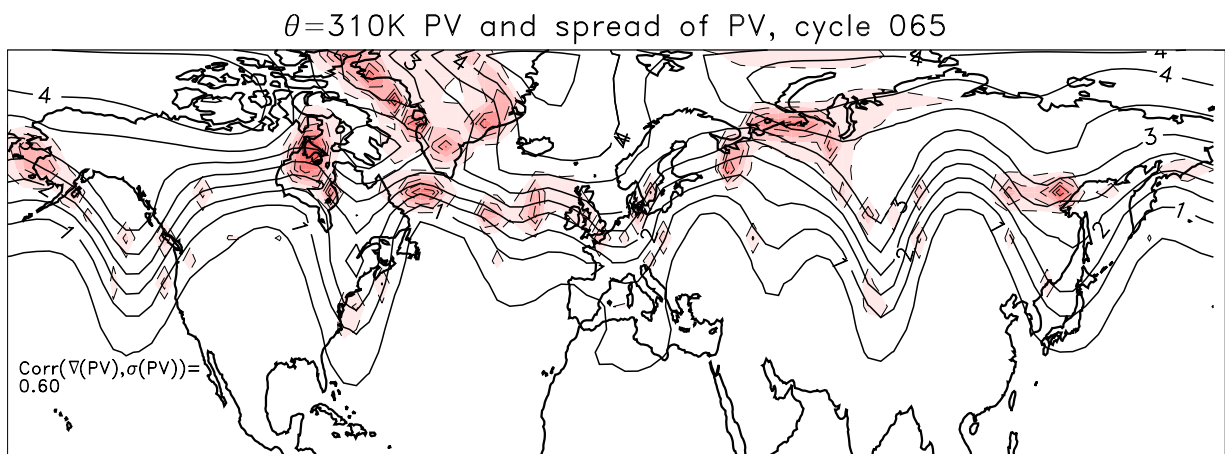


Figure 13. Potential vorticity of true state (solid lines) and ensemble standard deviation (dashed lines and shaded) of analysis potential vorticity for  $\theta=310K$  surface on day 32.5. True state PV is contoured at  $[0.5, 1.0, \dots] \times 10^{-7} K Pa^{-1} s^{-1}$  and spread at  $[1.0, 2.0, \dots] \times 10^{-8} K Pa^{-1} s^{-1}$ .

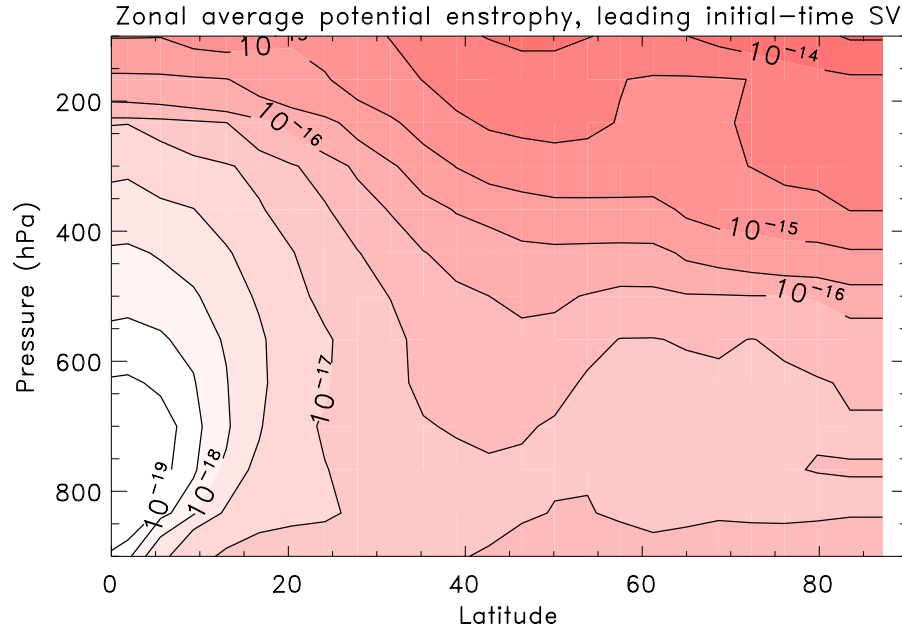


Figure 14. Zonal and time average of enstrophy (squared PV) of leading initial-time AEC SV.

Contours are logarithmically plotted. Units are  $K^2 Pa^{-2} s^{-2}$ .

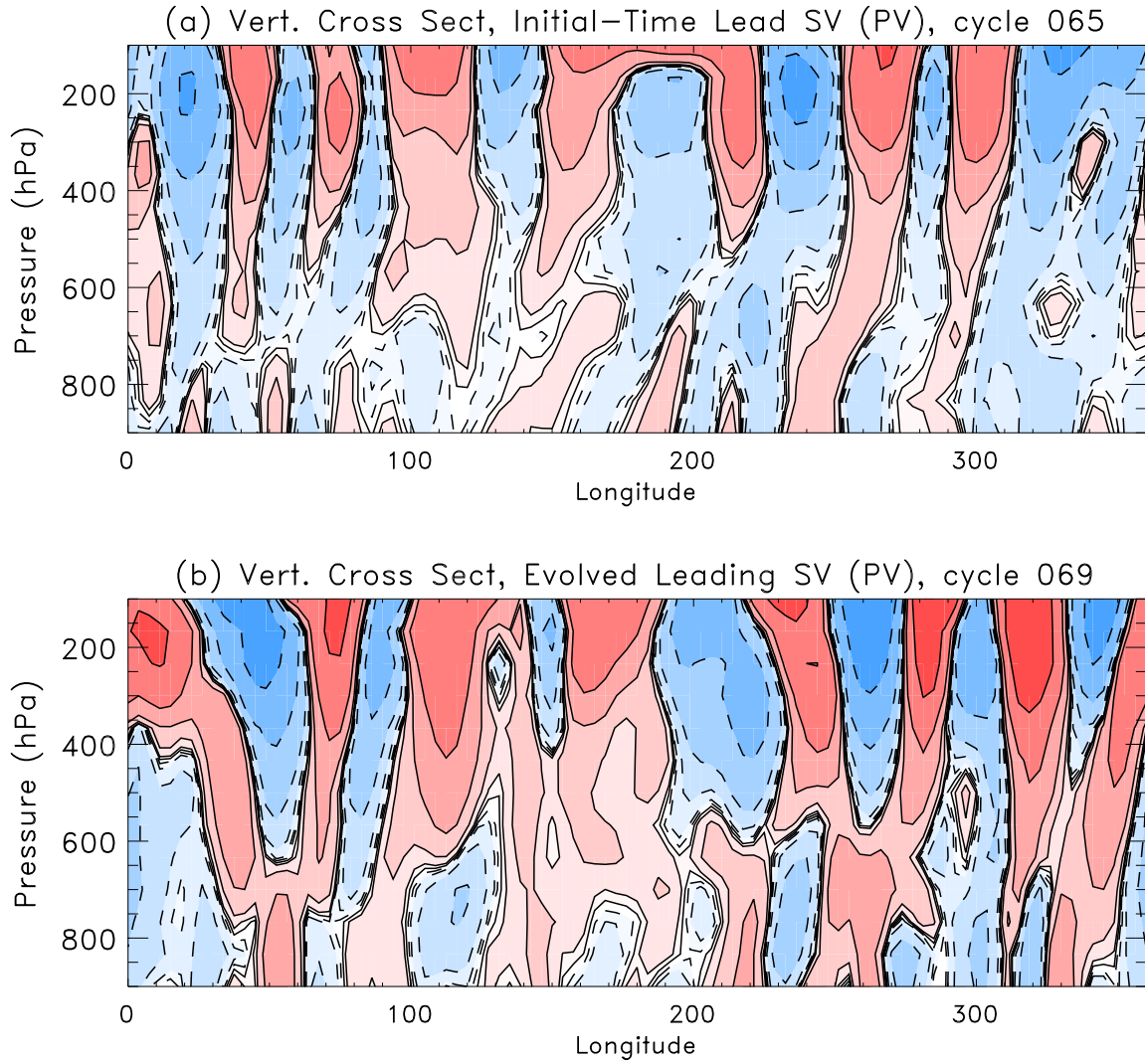


Figure 15. Vertical cross section of PV for the leading AEC SV for the case shown in Figs. 10, 11, and 13. The cross section is around a latitude circle at approximately  $42.5^\circ$  N. Contours are plotted logarithmically; every second contour is one order of magnitude change. Deeper colors denote larger values. (a) Initial-time AEC SV, and (b) evolved AEC SV.

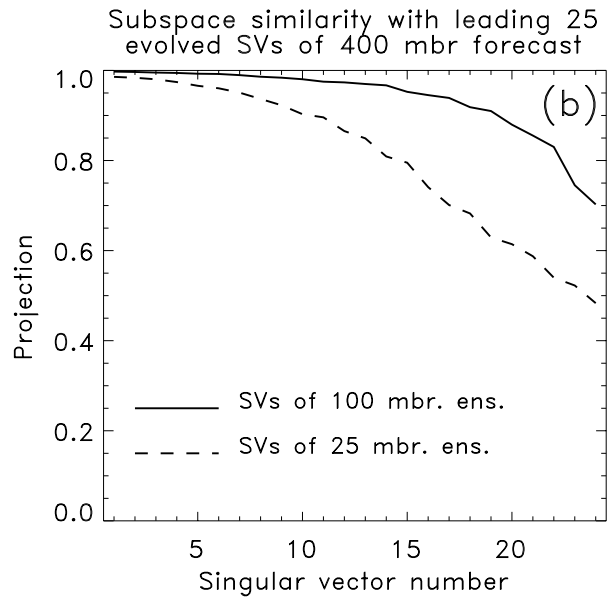
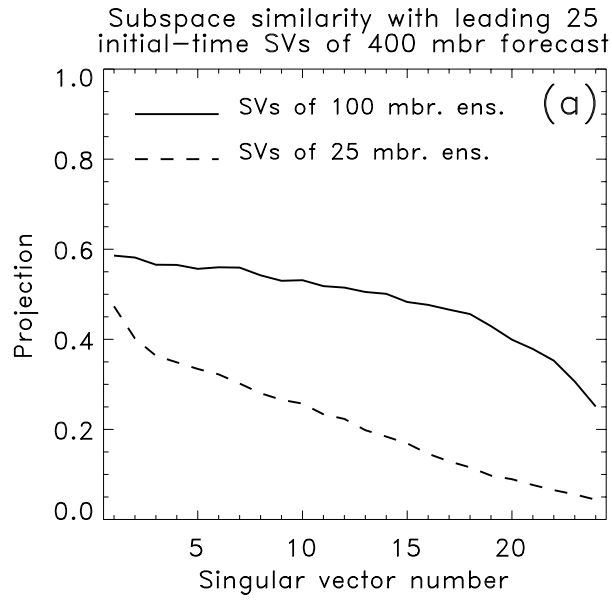


Figure 16. Subspace similarity of leading singular vectors from 25 and 100 member ensemble onto subspace of leading 25 singular vectors from 400-member ensemble. (a) Subspace similarity of initial-time singular vectors. (b) Subspace similarity of evolved singular vectors.